

# Janus Functionalized Boron-Nitride Nanosystems as a Potential Application for Absorber Layer in Solar Cells

Basant Roondhe,\* Vaishali Roondhe, Alok Shukla, Shobha Shukla, Wei Luo, Rajeev Ahuja,\* and Sumit Saxena\*

Janus nanosystems enable one to achieve complementary properties in a single entity. In the current study, the fundamental properties like structural, electronic, and dynamical of Janus hexagonal boron nitride (h-BN) by selectively hydrogenating and fluorinating a h-BN surface are systematically examined, using density functional theory. Functionalization of h-BN introduces partial  $sp^3$  (buckled) character in the predicted materials as compared to planar  $sp^2$  h-BNs. Fully fluorinated and hydrogenated h-BN have a direct bandgap of 3.42 and 3.37 eV, respectively. All the investigated configurations are predicted to be dynamically stable. Furthermore, optical properties including dielectric function, absorption spectra, refractive index, and reflectivity are evaluated to realize the optical and photocatalytic behavior of considered systems. The dielectric function  $\epsilon_2(\omega)$  shows fundamental absorption edge arising at 3.2, 3.9, 2.8, and 3.4 eV for hydrogen on boron and nitrogen, hydrogen on boron and fluorine on nitrogen, fluorine on boron and hydrogen on nitrogen (FBNH) and fluorine on boron and nitrogen which is comparable to the bandgap of respective monolayers. Solar cell parameters of all considered BN structures are calculated using the Shockley–Queisser (SQ) limit. The highest short-circuit current density ( $J_{sc}$ ) for FBNH is found to be  $2.1 \text{ mA cm}^{-2}$  providing the efficiency of 8.27% making FBNH a potential candidate for absorber layer in solar cells.

structural correspondence with graphene.<sup>[2]</sup> Contrary to graphene, h-BN consists of large bandgap ( $\approx 4.5\text{--}6 \text{ eV}$ ) due to ionic nature of the heteronuclear bonding between B and N.<sup>[3]</sup> Wide bandgap of h-BN restricts its utilization in electronic transport and energy conversion applications. The confinement in 2D materials results due change in their physical and chemical properties through strain, external fields, surface functionalization, etc.<sup>[4]</sup> Surface functionalization with hydrogen has been reported in many studies because of its possible existence on 2D surfaces during synthesis.<sup>[5]</sup> Studies show that functionalization of graphene on either or both sides modify its electronic properties significantly.<sup>[6]</sup> Fluorination and hydrogenation of 2D materials has led to unique and significant properties.<sup>[7]</sup> Recently, a new evolving category of 2D materials, “Janus” 2D materials, has gained significant consideration. “Janus” materials were first introduced in 1988 by observing a spherical glass droplet having asymmetric surface hydrophilicity.

Over the past 30 years many Janus materials have been fabricated to utilize in different applications.<sup>[8]</sup> The synthesis of Janus graphene has also been proposed by carrying out its asymmetric functionalization.<sup>[9,10]</sup>


Functionalizing different surfaces with different adatoms results in the development of Janus type polar single-layers. Janus

## 1. Introduction

The remarkable features of graphene have motivated the exploration of various 2D honeycomb structured materials via exfoliation out of their respective bulk form.<sup>[1]</sup> Among others, hexagonal boron nitride (h-BN) has gained considerable attention due to its

B. Roondhe, S. Shukla, S. Saxena  
Nanostructures Engineering and Modeling Laboratory  
Department of Metallurgical Engineering and Materials Science  
Indian Institute of Technology Bombay  
Mumbai, Maharashtra 400076, India  
E-mail: basant.roondhe@iitb.ac.in; sumit.saxena@iitb.ac.in

V. Roondhe, A. Shukla  
Department of Physics  
Indian Institute of Technology Bombay  
Mumbai, Maharashtra 400076, India  
W. Luo, R. Ahuja  
Condensed Matter Theory Group  
Materials Theory Division  
Department of Physics and Astronomy  
Uppsala University  
Box 516, Uppsala 75120, Sweden  
E-mail: rajeev.ahuja@physics.uu.se  
R. Ahuja  
Department of Physics  
Indian Institute of Technology Ropar  
Rupnagar, Punjab 140001, India

 The ORCID identification number(s) for the author(s) of this article can be found under <https://doi.org/10.1002/aelm.202300013>

© 2023 The Authors. Advanced Electronic Materials published by Wiley-VCH GmbH. This is an open access article under the terms of the Creative Commons Attribution License, which permits use, distribution and reproduction in any medium, provided the original work is properly cited.

DOI: 10.1002/aelm.202300013

structures are known to present remarkable characteristics, arising due to induced charge which make them useful for catalysis, sensors, drug delivery etc.<sup>[11]</sup> Janus materials have shown significant applications in solar cells due to their remarkable optical properties.<sup>[12,13]</sup> In the Janus monolayer the electron and the holes get separated due to intrinsic dipole formation. This occurs due to internal electric field between different surfaces which causes prominent band bending and can be utilized in efficient heterojunction photocatalysis.<sup>[14]</sup> In the last few years an exorbitant surge in energy requirement<sup>[15–17]</sup> has been observed globally. To fulfill these needs, fossil fuels such as coal, oil and natural gas have been exploited. However, with limited resources of fossil fuel and a cleaner environment, we need to swap them with greener and economical sources of renewable energy. With the sun not dying for at least a few billion years, solar energy with its limitless extent provides a potential alternative.<sup>[18–20]</sup> Several materials such as silicon,<sup>[21]</sup> perovskites,<sup>[22]</sup> organic solar cells<sup>[23]</sup> have been extensively developed for photovoltaic (PV) applications. Further modifications are increasing day-by-day to achieve higher efficiency along with low cost and non-toxicity using band gap engineering, functionalization and also through addition of quantum dots.<sup>[24–28]</sup> Boron nitride due to its wide band gap allows researchers to select suitable materials for functionalization to tailor its electronic properties. In a study done by Wu et al.<sup>[29]</sup> demonstrated the creation of Janus nanostructures by grafting together boron nitride (BN) and carbon nanotubes. By combining these two materials, the researchers were able to fine-tune the functionality of the resulting structures. While BN and C–C have similar geometrical arrangements, their electronic properties are vastly different due to their isoelectronic nature. By integrating BN into C nanostructures, the researchers were able to create anisotropic particles with exotic physical and chemical properties. A straightforward technique was introduced by Liu et al.<sup>[30]</sup> to modify the solubility of boron nitride nanosheets (BNNs) in different organic solvents using a “Janus” modifier, P(S-b-MMA). This method enabled the preservation of the 2D lattice integrity of BNNs, while simultaneously enhancing their processability in solution. Furthermore, P(S-b-MMA) served as a “Janus” compatibilizer by enhancing the compatibility between BNNs and diverse polymer matrices. Here, we report first principles studies using density functional theory (DFT) calculations to investigate the structural, dynamical, electronic, and optical properties of hydrogenated and fluorinated and Janus functionalized h-BN. Attributing to its tunable electronic and optical properties which is promising for photovoltaic application, we have also studied its solar cell parameters. Our studies revealed that selective surface functionalization through hydrogen and fluorine could tune the bandgap of h-BN significantly. In addition, hydrogenated, fluorinated and Janus functionalized 2D h-BN are dynamically stable. All monolayers considered in this study have had their solar cell parameters calculated according to the Shockley–Queisser (SQ) limit.<sup>[31,32]</sup> The short-circuit current density ( $J_{sc}$ ) of the HBNH (hydrogen on boron and nitrogen), HBNF (hydrogen on boron and fluorine on nitrogen), FBNH (fluorine on boron and hydrogen on nitrogen) and FBNF (fluorine on boron and nitrogen) monolayer was obtained around 0.636, 0.003, 2.15, and 0.545 mA cm<sup>−2</sup>, while the efficiency of these material was found to be around 2.53%, 0.02%, 8.27%, and 1.96%. The enhanced efficiency of FBNH suggests a promising application as an absorber

layer in solar cells. We believe that our work offers the possibility of using Janus BN based absorber layers in optoelectronic devices, and, therefore, will be useful for experimentalists.

## 2. Computational Methodology

The first-principles approach based on density functional theory (DFT) was employed for all calculations, using Quantum Espresso software<sup>[33]</sup> which employs plane-wave basis sets to expand the Kohn–Sham orbitals. Optimization was performed using the Broyden–Fletcher–Goldfarb–Shanno (BFGS) algorithm.<sup>[34]</sup> The exchange–correlation functional was treated using the Perdew–Burke–Ernzerhof (PBE) generalized gradient approximation (GGA), and ultrasoft pseudopotentials were utilized to account for the electrostatic interaction between ionic core and valence electrons.<sup>[35]</sup> An energy cutoff of 60 Ry and charge density cutoff of 600 Ry were used for electronic wave function. To avoid the interaction between periodic images, the supercell technique was employed with vacuum layers larger than 15 Å. Monkhorst–Pack<sup>[36]</sup> scheme was used to integrate the Brillouin zone (BZ) with k-mesh  $13 \times 13 \times 1$  for the unit cell. To solve the Kohn–Sham equation, Davidson’s iterative diagonalization method was utilized with an energy convergence threshold of  $1 \times 10^{-8}$  Ry. The Hellman–Feynman forces acting on each atom were less than 0.001 eV Å<sup>−1</sup>. Phonon properties were calculated using density functional perturbation theory (DFPT), as implemented in Quantum Espresso.<sup>[37]</sup> This approach enabled the calculation of phonons at any wave vector in the unit cell. A dense q-mesh of  $6 \times 6 \times 1$  was employed to compute the dynamical matrix for all considered 2D monolayers, while applying the acoustic sum rule for  $q \rightarrow 0$ . The dynamic stability across the entire Brillouin Zone (BZ) was ensured by utilizing the forces during the phonon frequency calculation by DFPT. The Kramers–Kronig transformation was used to calculate the optical properties within the random phase approximation (RPA).<sup>[38]</sup> Solar cell parameters such as open circuit voltage ( $V_{oc}$ ), short circuit current density ( $J_{sc}$ ), reverse saturation current density ( $J_0$ ), efficiency ( $\eta$ ), and fill factor (FF), the Shockley–Queisser (SQ) limit were computed for all the monolayers considered in this work.<sup>[31,32]</sup>

## 3. Results and Discussion

### 3.1. Structural Properties

The optimized structures are shown in **Figure 1** and optimized structural parameters are given in **Table 1**. The separation height between B and N planes is found to be 0.52, 0.47, 0.54, and 0.51 Å for HBNH, HBNF, FBNH, and FBNF respectively. In HBNH and FBNF, hydrogen and fluorine atoms are adsorbed onto the top site of B and N atoms, with H–B and H–N bond lengths of 1.20 and 1.03 Å, and F–B and F–N bond lengths of 1.35 and 1.44 Å, respectively. The bond lengths of H–B and F–N are larger than those of H–N and F–B, respectively, due to the differences in bonding between these atoms. It is clear from the Figure that all HBNH, HBNF, FBNH, and FBNF have slightly buckled honeycomb structures unlike h-BN and graphene, which have strictly planar structures.

In comparison with conventional 2D h-BN, the lattice constant “a” of HBNH, HBNF, FBNH, and FBNF is found to increase by

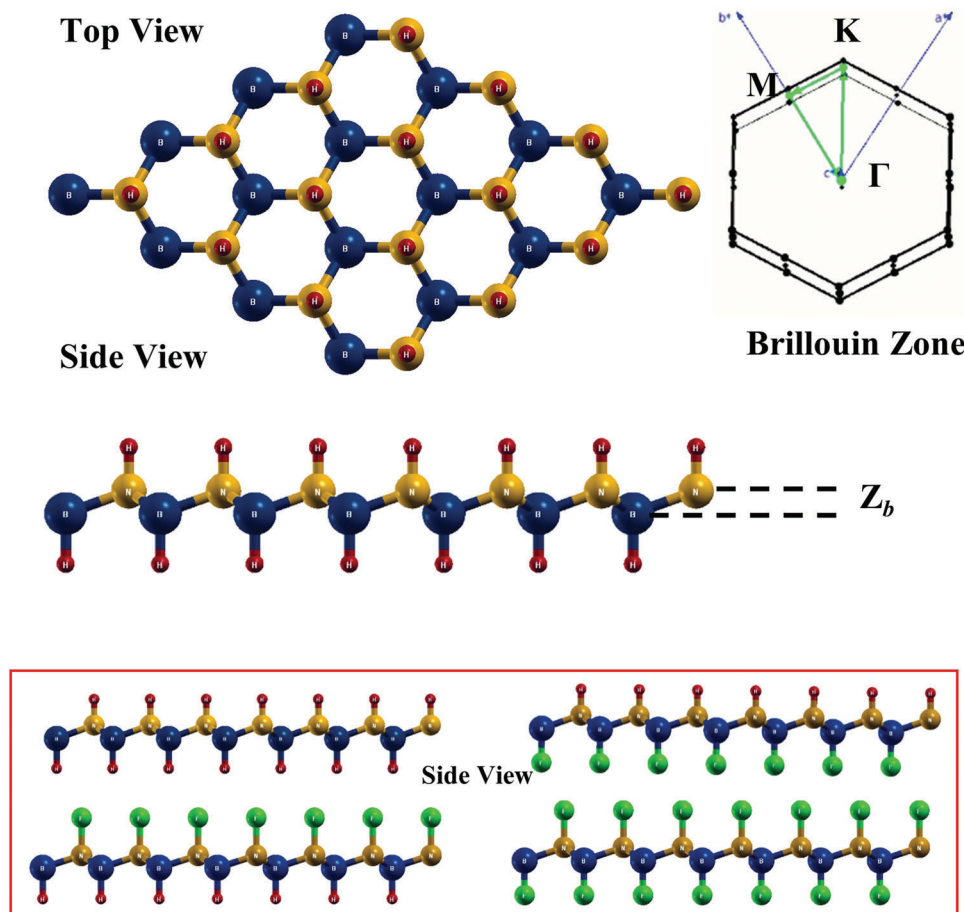


**Figure 1.** Crystal structure of Janus BN (top and side view) along with the first hexagonal Brillouin zone. The vertical distance ( $Z_b$ ) between B and N atoms in the unit cell is defined as buckling height. Lower panel shows the side view of optimized structures of HBNH, HBNF, FBNH, and FBNF. The blue, yellow, red, and green represents boron, nitrogen, hydrogen and fluorine atoms respectively.

2.87%, 3.58%, 4.78%, and 5.57% respectively. This could be attributed to the chemical bond formation between the h-BN sheet and H/F atoms. Increase in the bond length between B–N is also observed. The bond length between B–H/F or N–H/F are observed to be shorter as compared to B–N suggesting the strong covalent bonding. After the functionalization, the system (h-BN), the hybridization of system is found to change from  $sp^2$  to  $sp^3$  result-

ing in buckling of the sheets which distorts its planar geometry.<sup>[6]</sup> Calculated geometric parameters along with the buckling height have been tabulated in Table 1

The formation energy  $E_f$  are calculated using Equation (1)

$$E_f = \frac{1}{4} [E_{\text{total}} - E_B - E_N - nE_H - nE_F] \quad (1)$$

where  $E_{\text{total}}$  is the total energy of the Janus system,  $E_B$  and  $E_N$  is the total energy of individual B and N,  $E_H$ , and  $E_F$  are the total energies single H and F atom, respectively. Our observations indicate that all systems exhibit negative formation energy, which confirms their thermodynamic stability and suggests a feasible possibility of their experimental synthesis.

### 3.2. Dynamical Properties

Along with the dynamical stability, phonon dispersion curves (PDC) are useful in understanding the spectroscopic, mechanical, thermodynamical and acoustic characteristics of materials at finite temperatures. The insights regarding the dynamical stability are given through the PDC evaluated by dynamical matrix diagonalization (DMD). The calculated PDCs for HBNH, Janus

**Table 1.** Lattice constants “a,” bond lengths between B–N ( $d_{B-N}$ ), B–H ( $d_{B-H}$ ), N–H ( $d_{N-H}$ ), B–F ( $d_{B-F}$ ), and N–F ( $d_{N-F}$ ), buckling height ( $Z_b$ ), and formation energies ( $E_f$ ) of Janus BN.

XBNX	HBNH	HBNF	FBNH	FBNF
$a$ [Å]	2.58	2.60	2.64	2.66
$d_{B-N}$ [Å]	1.58	1.57	1.62	1.62
$d_{B-H}$ [Å]	1.20	1.20	–	–
$d_{N-H}$ [Å]	1.03	–	1.03	–
$d_{B-F}$ [Å]	–	–	1.34	1.35
$d_{N-F}$ [Å]	–	1.46	–	1.44
$Z_b$ [Å]	0.52	0.47	0.54	0.51
$E_f$ [eV]	–4.36	–4.01	–4.89	–4.50

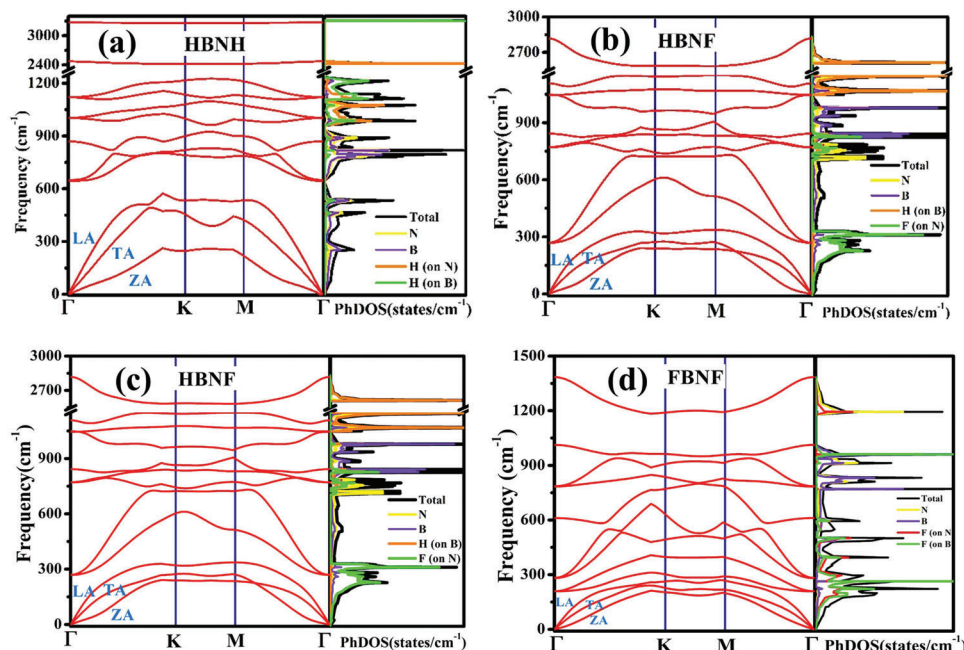


**Figure 2.** Phonon dispersion along high symmetry direction  $\Gamma$ -K-M- $\Gamma$  for a) HBNH, b) HBNF, c) FBNH, and d) FBNF systems.

HBNF, Janus FBNH and FBNF in high symmetry direction  $\Gamma$ -K-M- $\Gamma$  of the Brillouin zone (BZ) laterally with the partial phonon density of states (PhDOS) are presented in **Figure 2**. The phonon analysis indicate that all considered systems are dynamically stable because there are no imaginary frequencies in their PDCs. The total number of branches in PDCs is directly related to the number of atoms in the unit cell of material. The unit cell of HBNH, HBNF, FBNH, and FBNF contains 4 atoms with P-3m1 symmetry, the PDC have 12 phonon modes (3 acoustic and 9 optical). The acoustic modes comprising longitudinal acoustic (LA) and transverse acoustic (TA) modes present dispersion linearly nearby  $\Gamma$  point. However, the characteristic nature of 2D materials is given by out-of-plane acoustic (ZA) mode displaying quadratic dispersion.<sup>[39,40]</sup> The quadratic dispersive nature of out-of-plane acoustic (ZA) mode can be understood due to the vibrations caused at the lowest amplitude, strain energy, which in turn is linked with curling of out-of-plane acoustic (ZA) mode in 2D materials.<sup>[41]</sup> It is significant to note that contrary to graphene, all considered monolayer show buckling due to coupling of the ZA with TA and LA modes.

Under zero strain conditions and with wave vectors near the zone center, the ZA branch exhibits quadratic behavior, which signifies a loss of 2D ordering. Consequently, the ZA mode is widely employed to comprehend rippling in 2D materials.<sup>[42–43]</sup>

Based on **Figure 2**, it is noted that in spite of the similar geometrical structure of HBNH, HBNF, FBNH, and FBNF, there are dissimilarities in phonon-dispersion curves. The ZA mode is linked with stiffness and lattice heat capacity of the monolayer in long-wavelength region. Furthermore, softening of TA and LA modes is noticed, representing reduction in the group velocities. Contrary to TA and LA modes, ZA mode comprises smaller group velocity attributed to the fact of parabolic dispersion around  $\Gamma$  point. Moreover, because of the low mass difference, no gap is observed amongst acoustic and optical branches.

The highest phonon frequencies for HBNH, HBNF, FBNH, and FBNF at  $\Gamma$  point are  $\approx 3300$ ,  $2850$ ,  $3370$ , and  $1380$   $\text{cm}^{-1}$  respectively, indicating that all the studied systems kinetically stable. The PDCs of HBNH, FBNH, and HBNF can be separated into three frequency groups; low, midway and high respectively. In case of FBNF there is no such gap between low and mid frequencies thus it has only low and suppressed high frequency, range which can be attributed to the weak harmonic force constant and increased mass density. In PDCs of HBNH, HBNF, FBNH, and FBNF, at  $\Gamma$  point, three singly (A) and three doubly (E) degenerated optical phonon modes are observed, i.e.,  $\Gamma = 3A + 3E$ . All 12 modes in HBNH, HBNF, FBNH, and FBNF are likewise distributed. For FBNF the modes are distributed in  $0$  to  $\approx 1500$   $\text{cm}^{-1}$  frequencies ranging while in case of HBNH, HBNF, FBNH they are distributed in the range  $0$  to  $\approx 3400$   $\text{cm}^{-1}$ . Also, the optical phonons frequencies values shift to higher frequencies in HBNH, HBNF, and FBNH monolayers as a result of the lower average atomic mass of the unit cell. The stability was also confirmed by calculating the projected phonon density of states (PhDOS), as shown in the right panel of **Figure 2**. Atom-specific contributions to phonon modes are better understood in terms of PhDOS (**Figure 2**). The PhDOS is a significant characteristic involving phonon frequencies in the entire BZ given as the equation<sup>[44]</sup>

$$g(\omega) = \frac{1}{N} \int_{\text{BZ}} \sum_j \delta[\omega - \omega_j(\vec{q})] d\vec{q} \quad (2)$$

Here,  $N$  be the normalization constant so that  $\int g(\omega) d\omega = 1$ . Here  $g(\omega) d\omega$  is the ratio of number of eigen states in frequency interval  $(\omega, \omega + d\omega)$  to the total number of eigenstates, while  $\omega_j(\vec{q})$  is the phonon frequency of  $j$ th phonon mode. Dispersive nature is presented in the lower frequency area due to nearby



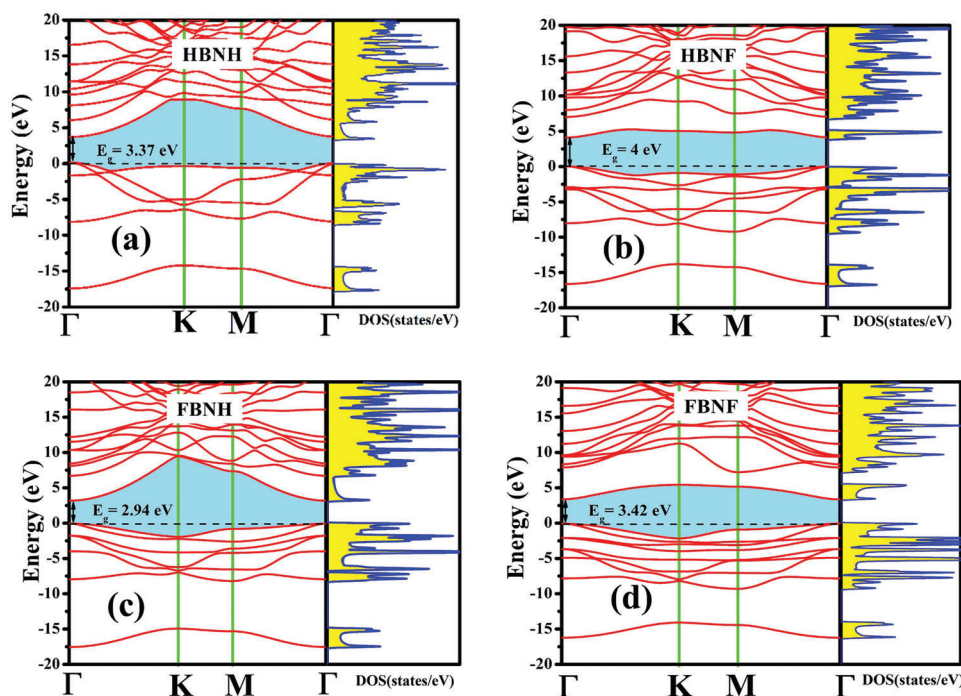


**Figure 3.** Calculated electronic band structure along the  $\Gamma \rightarrow K \rightarrow M \rightarrow \Gamma$  direction and density of states (DOS) of a) HBNH, b) HBNF, c) FBNH, and d) FBNF. The zero energy value corresponds to the Fermi level.

distribution of potential energy in several modes. As the dispersion nature is dependent on atomic interaction strength, additionally, various variations in the modes mainly depends on mixing nature of modes due to repulsion. The strong peaks in Ph-DOS arises due to flat bands in the PDCs. Additionally, weak singularity in low frequency area is because of certain highly dispersed acoustical and low frequency optical phonon modes. Because of small mass of boron and nitrogen atom a sharp peak of fluorine vibration can be seen in DOS in acoustic region of HBNF, FBNH, and FBNF while in case of HBNH the domination in the acoustic region is due to nitrogen suggesting their maximum contribution. In case of FBNF, we witness that the occurrence of fluorine atom in z-direction leads to suppression of higher optical vibrational frequencies ( $\approx 1300 \text{ cm}^{-1}$ ) compared to those in HBNF, FBNH, and HBNH ( $\approx 2800$ ,  $\approx 3400$ , and  $\approx 3300 \text{ cm}^{-1}$ ). One should further note from the PDCs of HBNF, FBNH, and FBNF that the frequencies of the acoustic modes in phonon are suppressed as compared to HBNH. This decrease in acoustic mode of HBNF, FBNH, and FBNF can be accredited to the addition of fluorine in the unit cell, which additionally reduces harmonic force constant and increases the mass density in HBNF, FBNH, and FBNF.<sup>[45]</sup> We can understand and easily identify the high frequency phonons ( $3300$ ,  $3370$ , and  $2850 \text{ cm}^{-1}$ ) corresponding to H modes due to B–H stretching in case of HBNH and HBNF and N–H stretching in case of FBNH. The acoustic region in the PDCs is dominated by B and N in case of HBNH while in case for HBNF, FBNH, and FBNF it is dominated by F. On the other hand, the midway frequency region is dominated by B, N, and F. There are no imaginary frequencies in PDC and Ph-DOS confirming dynamical stability of HBNH, HBNF, FBNH, and FBNF, and also suggesting the possibility of forming free standing monolayers of Janus BN systems.

### 3.3. Electronic Properties

The electronic band structures, was calculated along high symmetry direction  $\Gamma$ –K–M– $\Gamma$  in the Brillouin zone for all HBNH, HBNF, FBNH, and FBNF systems, and are presented in **Figure 3**.

As can be seen from the figure, all the systems under consideration exhibit semiconductor behavior, with their valence band maxima (VBM) and conduction band minima (CBM) situated at  $\Gamma$ , indicative of a direct bandgap. Bandgap of 3.37, 4, 2.94, and 3.42 eV are observed for HBNH, HBNF, FBNH, and FBNF, respectively, and which is much smaller than that of h-BN (4.9 eV).<sup>[45]</sup>

Two H atoms and F atoms introduce two occupied energy bands, one in majority and the other one in the minority sector sharing the same energy. These bands are located just above the valence band of pristine BN sheet, as a result of which the band gap of the system is reduced. Chemical functionalization can lead to an increase in the buckling height ( $\Delta h$ ) between the B and N atoms in a BN monolayer, which arises from the formation of H–B (F–B) and H–N (F–N) bonds. Additionally, our findings reveal a transformation of the planar  $sp^2$  hybrid orbitals to  $sp^3$ -like orbitals following chemical functionalization. Moreover, a high  $\Delta h$  value results in strong anisotropy, as previously reported.<sup>[46]</sup> And also, in case of  $sp^3$  hybridization, a barrier is introducing which restrict the electron flow by opening a band gap thereby yielding the generation of insulating and semiconducting regions in 2D system.<sup>[47]</sup> As far as the electronic density of states is concerned, we find that most of the contribution near the Fermi level comes from B and N atoms in case of HBNH, HBNF, and FBNH. However, in case of FBNF, most of the contribution near the Fermi level is due to the F atom.

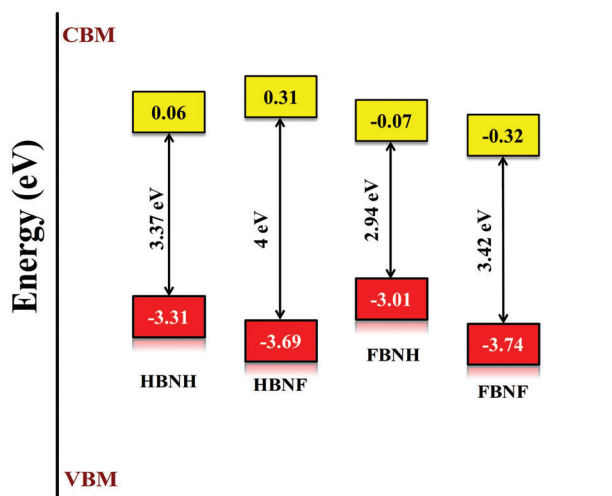


Figure 4. Energy level alignment of VBM and CBM energy levels.

We believe that the direct and smaller band gap suggest that the material has a strong potential in novel optoelectronics, photocatalysis, thermoelectric as well as solar cell application. The energy level alignment of the valence band maximum (VBM) and conduction band minimum (CBM) is altered by the formation of polar covalent bonds, such as  $N^+-H^+$  or  $N^+-F^-$ , resulting from H and F functionalization, as depicted in Figure 4.

### 3.4. Optical Properties

To calculate the optical parameters, photon energy values ranging from 0 to 25 eV were considered. Additionally, for all optical parameters, the electric vector ( $E$ ) was oriented both perpendicular and parallel to the  $Z$ -axis. The dielectric function for the optical parameters can be described as  $\epsilon(\omega) = \epsilon_1(\omega) + i\epsilon_2(\omega)$ , in which  $\epsilon_2(\omega)$  is the imaginary part of the dielectric function which can be obtained by using the optical matrix elements from the electronic band structure and the  $\epsilon_1(\omega)$  which is the real part of dielectric function can be obtained by the Kramers–Kronig relationship<sup>[48,49]</sup>

$$\epsilon_2(\omega) = \frac{2e^2\Pi}{\Omega\epsilon_0} \sum_{k, c, v} \int |\psi_k^c \langle \hat{u}r \rangle \psi_k^v|^2 \delta(E_k^c - E_k^v - E) \quad (3)$$

In the above equation, “ $\omega$ ” is the frequency, “ $e$ ” is the charge on electron, and  $\Omega \propto m^2\omega^2$ , where  $m$  is the effective mass of an electron, and  $\psi_k^c$  and  $\psi_k^v$  are the conduction and valence bands wave function at  $k$ , respectively. From the equation, it is clear that the imaginary part depends on the momentum matrix element and joint density of states (JDOS) which is mainly several possible transitions between the valence band and the conduction band. The real part of the dielectric function can be calculated by using below equation

$$\epsilon_1(\omega) = 1 + \frac{2}{\pi} P \int \frac{\omega' \epsilon_2(\omega')}{\omega'^2 - \omega^2} d\omega' \quad (4)$$

As previously mentioned the below equation defines the dielectric function

$$\epsilon(\omega) = \epsilon_1(\omega) + i\epsilon_2(\omega) \quad (5)$$

Now,  $\epsilon_1 = n^2 + k^2$  and  $\epsilon_2 = 2nk$  are the conditions which must be satisfied by the above equations, where  $n$  and  $k$  are nothing but the refractive index and extinction coefficient, respectively. Both of these quantities can be obtained by using the dielectric function  $\epsilon(\omega)$ , as given below

$$n(\omega) = \frac{1}{\sqrt{2}} \left[ (\epsilon_1^2 + \epsilon_2^2)^{\frac{1}{2}} + \epsilon_1 \right]^{\frac{1}{2}} \quad (6)$$

and

$$k(\omega) = \frac{1}{\sqrt{2}} \left[ (\epsilon_1^2 + \epsilon_2^2)^{\frac{1}{2}} - \epsilon_1 \right]^{\frac{1}{2}} \quad (7)$$

And now by using the values of  $n(\omega)$  and  $k(\omega)$  we can further obtain the values of absorption coefficient  $\alpha(\omega)$  and reflectivity  $R(\omega)$ , respectively, using below equations

$$\alpha(\omega) = \frac{\omega k}{c} = \frac{4\pi k}{\lambda_0} \quad (8)$$

$$R(\omega) = \frac{[(n-1)^2 + k^2]}{[(n+1)^2 + k^2]} \quad (9)$$

In the above Equations (8) and (9) the  $\lambda_0$  is the velocity of light and the  $k$  is the extinction coefficient. We have also calculated the energy loss function  $L(\omega)$ , which arises due to the motion of electrons in the semiconductor, by dielectric functions using below expression

$$L(\omega) = \frac{\epsilon_2(\omega)}{\epsilon_1^2(\omega) + \epsilon_2^2(\omega)} \quad (10)$$

The subsequent Figures 5a–d and 6a–d, illustrate the optical response of the complex dielectric function  $\epsilon(\omega)$  of HBNH, HBNF, FBNH, and FBNF, including the real and imaginary components. It is known that the imaginary component  $\epsilon_2(\omega)$  of the dielectric constant is determined by the interband transitions of electrons from the valence bands to the conduction bands, whereas the real component  $\epsilon_1(\omega)$  of the dielectric function provides information on the electronic polarizability of the material through the Clausius–Mossotti relation.<sup>[50]</sup>

#### 3.4.1. Real Part

The optical response of incident light to HBNH, HBNF, FBNH, and FBNF represents high degree of anisotropy mainly within the region from infrared (IR) to vacuum UV-energy span ( $E < 13$  eV) on the other hand at higher energies the isotropic response is observed (see Figure 5). The static dielectric constants  $\epsilon_1(0)$  are (2.00, 1.90), (2.80, 2.00), (1.90, 1.80), and (2.50, 1.95) along both  $E \perp Z$  and  $E \parallel Z$  type of electric vector for HBNH, HBNF, FBNH, and FBNF monolayers, respectively. This variation of  $\epsilon_1(0)$  for HBNH, HBNF, FBNH, and FBNF is  $\epsilon_1(\text{FBNH}) < \epsilon_1(\text{HBNH}) < \epsilon_1(\text{FBNF}) < \epsilon_1(\text{HBNF})$ . The parallel radiation is comparatively significant than the perpendicular radiation which brings us to realized that HBNH, HBNF, FBNH, and FBNF may be useful

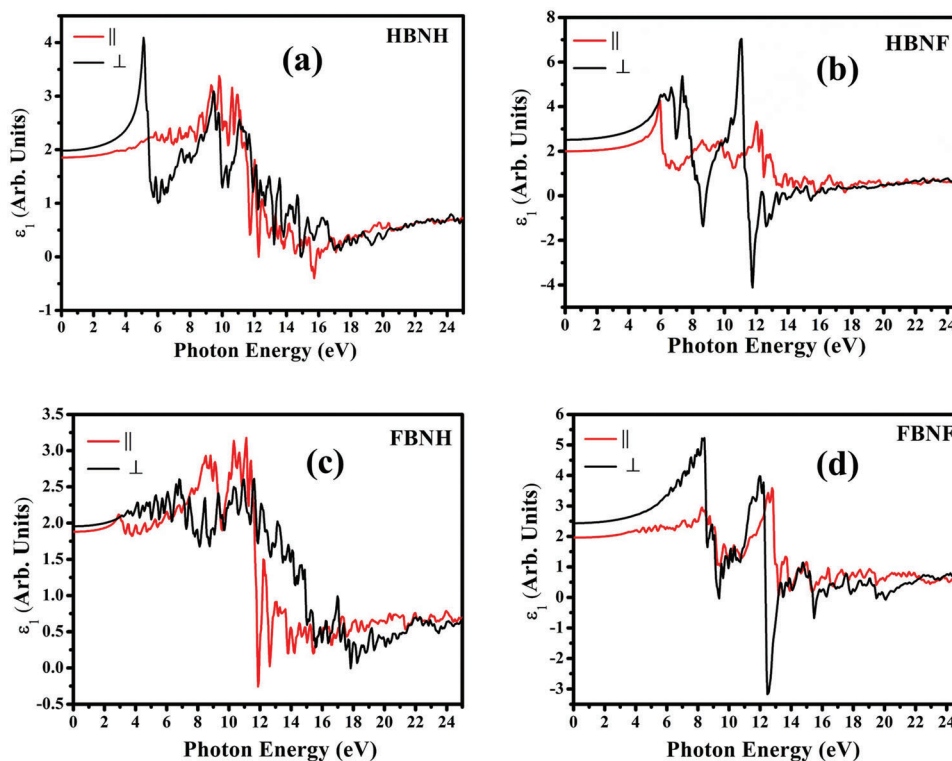


**Figure 5.** The real part of the calculated dielectric constant along with the parallel and perpendicular directions of a) HBNH, b) HBNF, c) FBNH, and d) FBNF.

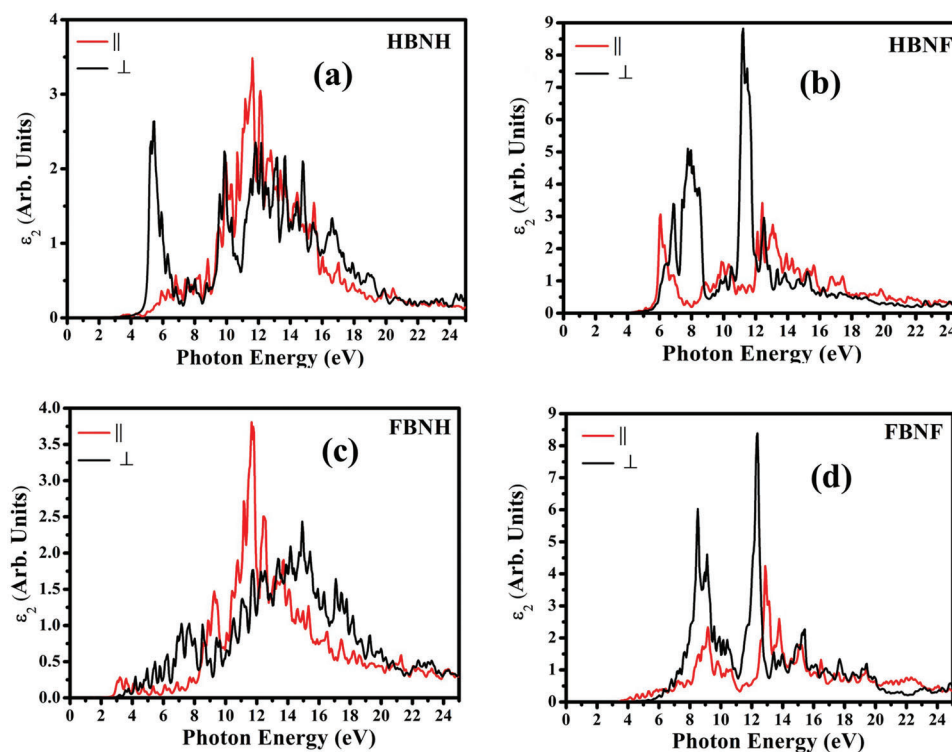


**Figure 6.** The imaginary part of the dielectric constant along with the parallel and perpendicular directions of a) HBNH, b) HBNF, c) FBNH, and d) FBNF.

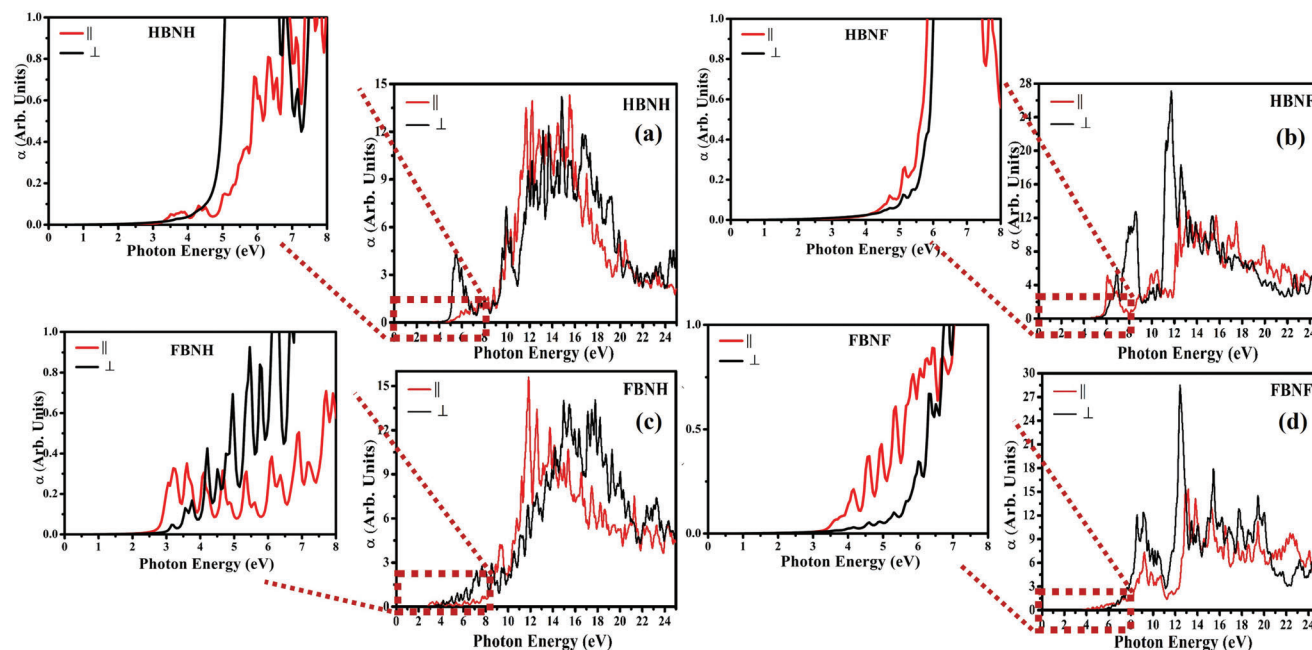


**Figure 7.** The absorption coefficient with the parallel and perpendicular directions of a) HBNH, b) HBNF, c) FBNH, and d) FBNF. Inset shows the zoom in image of absorption coefficient.

in solar cell applications.<sup>[51,52]</sup> Similarly, the real part shows the negative values into high energy region within 8–13 eV which illustrates the metallic character of HBNH, HBNF, FBNH, and FBNF monolayers in X-ray region of electromagnetic spectrum. Furthermore, in  $\epsilon_1(\omega)$ , negative values specify the negligible transmission of light in the deep X-ray region, suggesting optical transparency of these monolayer about 8–13 eV energy range.

### 3.4.2. Imaginary Part

We present our calculated imaginary part of the dielectric function  $\epsilon_2(\omega)$  for HBNH, HBNF, FBNH, and FBNF in Figure 6a–d. The main peaks of HBNH, HBNF, FBNH, and FBNF initiated mainly due to the electronic transition from the hybridized bonding between B 2p and N 2p and F 2p and H 1s states. The dielectric function  $\epsilon_2(\omega)$  indicates the fundamental absorption edge which is arising at 3.2, 3.9, 2.8, and 3.4 eV for HBNH, HBNF, FBNH, and FBNF, respectively. The absorption edge is arising when the electron has a direct transition between the highest valence band and the lowest conduction band.<sup>[53]</sup> Furthermore, the hybridized  $\pi$  and  $\sigma$  bonding-antibonding nature of 2p orbitals creates smaller amplitude peaks.

### 3.4.3. Absorption Coefficient

The realization for the photovoltaic conversion applications of these material can be achieved by calculating the absorption coefficients in the full spectrum range (IR to extreme UV). The absorption coefficient tells us about absorption capability of any material and range concerning incident radiation that could be solar. The absorption coefficients in parallel and perpendicular (direction of the plane) factors of the electromagnetic waves for HBNH,

HBNF, FBNH, and FBNF monolayer up to 25 eV are presented in Figure 7a–d. It is apparent from Figure 7a–d that anisotropic behavior is found for absorption coefficients. The edge of absorption occurs at 3.2, 3.9, 2.8, and 3.4 eV for HBNH, HBNF, FBNH and FBNF, respectively. The edge of absorption is similar to that of the imaginary parts of the dielectric function. The results suggest that these monolayers can be utilized for effective photovoltaic conversion.

Below the range of edge, these monolayers show transparent nature which results in low reflectivity. The absorption reduces to smaller value after 25 eV confirming complete transparency in far UV region. To further understand the absorption spectra, we have investigated the involvement of orbitals in one-electron transitions, leading to the following three peaks: the first peak, the second peak, and the most intense peak in the optical absorption spectra of HBNH, FBNF, and Janus BN (HBNF and HBNF), and present it in Table 2. We note that for all considered monolayers HBNH, FBNF, and Janus BN (HBNF and HBNF) the first peak is the result of the orbital transition  $|V \rightarrow C\rangle$ , at the  $\Gamma$  point, where V, and C, respectively, denote the top of the valence band and the bottom of the conduction band. The second peak for HBNH is because of the transition  $|V-1 \rightarrow C\rangle$ , at the  $\Gamma$  point. For FBNF transition  $|V \rightarrow C\rangle$ , from M to  $\Gamma$  point is responsible for the second peak. In case of Janus BN, i.e., HBNF transition  $|V \rightarrow C\rangle$  from M to  $\Gamma$  point contributes in the increment of second peak, while the equivalent peak for FBNH is due to transitions  $|V \rightarrow C\rangle$  from K to  $\Gamma$  point. The optical transitions exist at  $\Gamma$  point, or between M- $\Gamma$  and K- $\Gamma$  at the edge of Brillouin zone respectively. Lastly, we further examine the optical transitions of the maximum intensity peaks which are positioned at higher energies. Due to higher energy values (see Table 2), the transitions are noticed from the bands afar from the Fermi level.



**Table 2.** The optical absorption spectra of HBNH, FBNF, and Janus BN (HBNF and HBNF) show the first, second, and most intense peaks, along with the involved bands in the transition. The valence band maxima and conduction band minima are denoted by V and C, respectively. Furthermore,  $V - n$  ( $C + n$ ) represents the  $n$ th valence (conduction) band, counting from the Fermi level.

System	First peak position [eV]	Second peak position [eV]	Most intense peak position [eV]
HBNH	3.5 ( $ V \rightarrow C \rangle$ )	5.3 ( $ V-1 \rightarrow C \rangle$ )	12.8 ( $ V-3 \rightarrow C+6 \rangle$ )
HBNF	4.5 ( $ V \rightarrow C \rangle$ )	5.2 ( $ V \rightarrow C \rangle$ from M to $\Gamma$ )	12.5 ( $ V-3 \rightarrow C+4 \rangle$ )
FBNH	3 ( $ V \rightarrow C \rangle$ )	3.7 ( $ V \rightarrow C \rangle$ from K to $\Gamma$ point)	11.5 ( $ V-6 \rightarrow C \rangle$ )
FBNF	3.5 ( $ V \rightarrow C \rangle$ )	4.5 ( $ V \rightarrow C \rangle$ , from M to $\Gamma$ )	13 ( $ V-7 \rightarrow C+3 \rangle$ )

### 3.4.4. Refractive Index

The polarization of the material due to the incident electromagnetic wave give rise to the microscopic phenomenon, refractive index  $n(\omega)$ . The refractive indices are displayed in **Figure 8a–d** for HBNH, HBNF, FBNH, and FBNF. The minimum static refractive index ( $n(\omega) \perp Z$  and  $n(\omega) \parallel Z$ ) is (1.40, 1.35), (1.60, 1.40), (1.35, 1.30), and (1.65, 1.45) for HBNH, HBNF, FBNH, and FBNF monolayer, respectively. The smooth increase of refractive index  $n(\omega)$  is observed increase in the energy from IR region to UV region while decreases with few oscillations in extreme UV and above area. The maximum refractive index can be found from the magnitude of the peak, high peak value reveals higher refractive index of HBNH, HBNF, FBNH, and FBNF monolayer. The peak value is 2.10, 2.85, 1.70, and 2.40 at energy 5.00, 11.10, 7.20, and 8.30 eV for HBNH, HBNF, FBNH, and FBNF, respectively.

FBNH, and FBNF, respectively. The peak of refractive index of HBNH and HBNF falls in the UV region while for FBNH and FBNF the peak falls in extreme UV region. Therefore, the maxima move from UV region to extreme UV region is concluded. The high refractive index of HBNH, HBNF, FBNH, and FBNF specifies heat protection properties useful in maintaining constant temperature conditions for materials.<sup>[54]</sup> The degree of birefringence exhibited by materials can be estimated by examining the difference between the in-plane and perpendicular refractive indices. The anisotropic optical response of these monolayers accounts for their unique nonlinear optical properties. The values of  $\Delta n(0)$  are negative for all considered BNs, as shown in the data: HBNH (−0.05), HBNF (−0.2), FBNH (−0.05), and FBNF (−0.2). This satisfies the noncritical phase matching (NCPM) criterion, which is useful for achieving high system laser performance.

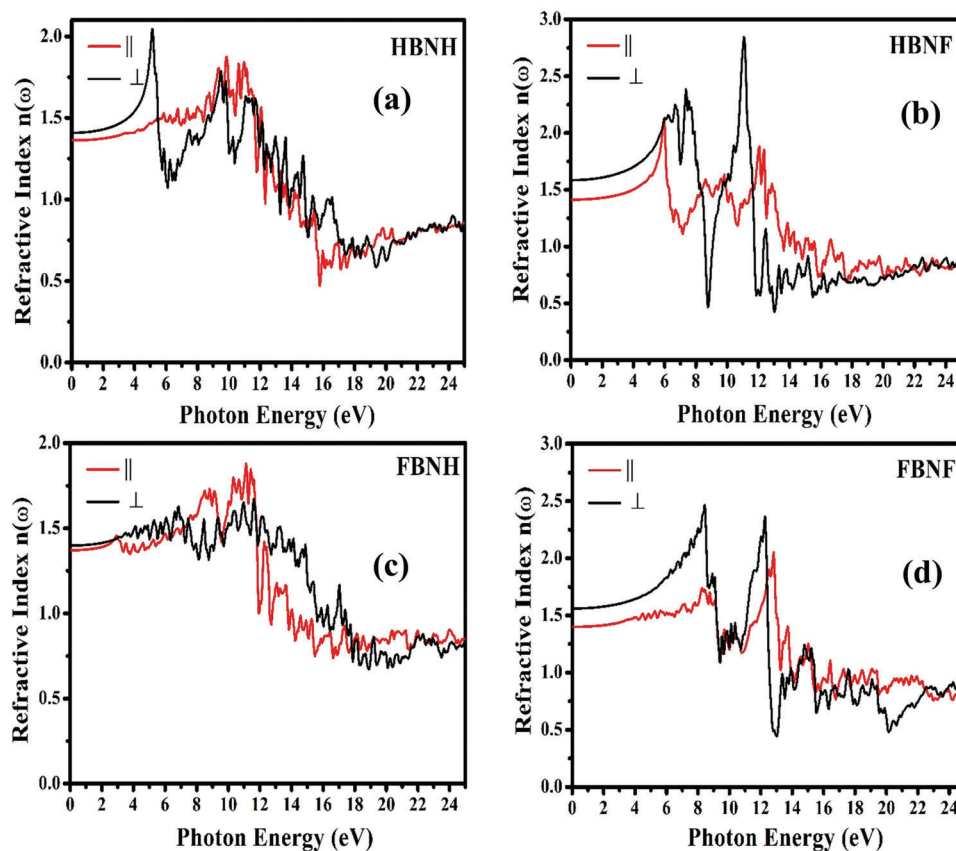


**Figure 8.** The refractive indices with the parallel and perpendicular directions of a) HBNH, b) HBNF, c) FBNH, and d) FBNF.

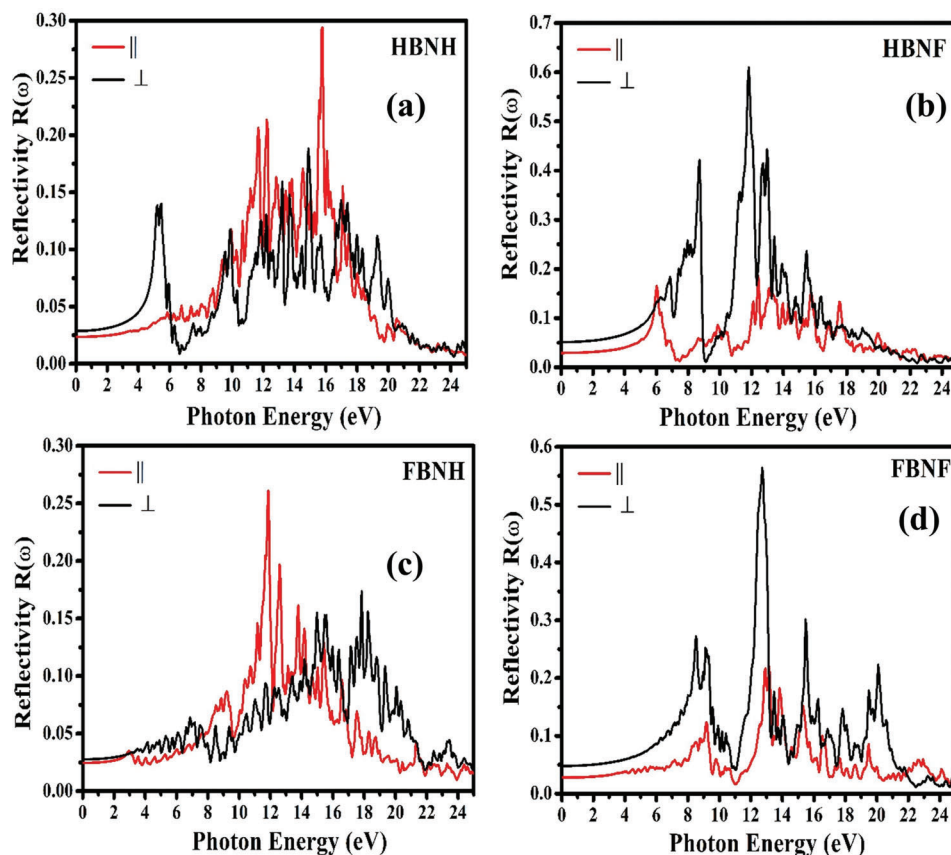


**Figure 9.** Reflectivity spectra  $R(\omega)$  with the parallel and perpendicular directions of the electric field polarization in a) HBNH, b) HBNF, c) FBNH, and d) FBNF.

### 3.4.5. Reflectivity

**Figure 9a–d** shows the parallel ( $R(\omega) \parallel Z$ ) and perpendicular ( $R(\omega) \perp Z$ ) electric field polarization of reflectivity of HBNH, HBNF, FBNH, and FBNF. The reflectivity spectra specify that the reflectivity of HBNH, HBNF, FBNH, and FBNF rises in the UV region, although it is minimizing in the IR region. It is notable that both the HBNH and FBNH show significantly high reflectivity initially ranging 4–6 eV and then in extreme UV range, while HBNF and FBNF displays high reflectivity in the range of 7–9 and 12–14 eV. The static part of reflectivity, at zero energy can be observe in Figure 9a–d, after that it starts increasing with some oscillations and at higher energy it vanishes (see Figure 9a–d). The reflectivity is majorly observed in the ultraviolet region for all these compounds suggesting their utilization as Bragg's reflectors.

### 3.4.6. Loss Spectra

The loss spectra of HBNH, HBNF, FBNH, and FBNF relative to the photon energy up to 25 eV are provided in **Figure 10a–d**. The energy loss spectrum is given through energy loss when an electron traveling through the homogeneous material. Figure 10a–d presents the threshold of the absorption edge occurring at 4.83, 5.98, 3.1, and 5.7 eV for HBNH, HBNF, FBNH, and FBNF re-

spectively. From Figure 10a–d, displays the wide plasma peaks primarily found in the extreme higher energy ranging between 18 and 22 eV for HBNH, HBNF, FBNH, and FBNF. Present investigation specifies the least energy loss by the electrons in the visible region for HBNH, HBNF, FBNH, and FBNF, signifying their application in optoelectronic devices.

### 3.5. Solar Cell Parameters

For material's application in solar cell, the solar cell parameters for instance open circuit voltage ( $V_{oc}$ ), short circuit current density ( $J_{sc}$ ), fill factor (FF) and power conversion efficiency (PCE,  $\eta$ ) have been evaluated through Shockley–Queisser (SQ) limit. The PCE is calculated using below equation<sup>[55]</sup>

$$\eta = \frac{FF \cdot J_{sc} \cdot V_{oc}}{P_{in}} \quad (11)$$

where  $P_{in}$  is total incident solar energy density ( $P_{in} = 1000 \text{ W m}^{-2}$ ). The parameter  $V_{oc}$ , stated as solar cell's maximum voltage occurring at zero current, is calculated using equation<sup>[56–58]</sup>

$$V_{oc} = E_{LUMO}^{Janus-BN} - E_{CB}^{TiO_2} \quad (12)$$

Above  $V_{oc}$  is the energy change among LUMO of considered monolayers and conduction band of acceptor  $TiO_2$ . The totality of

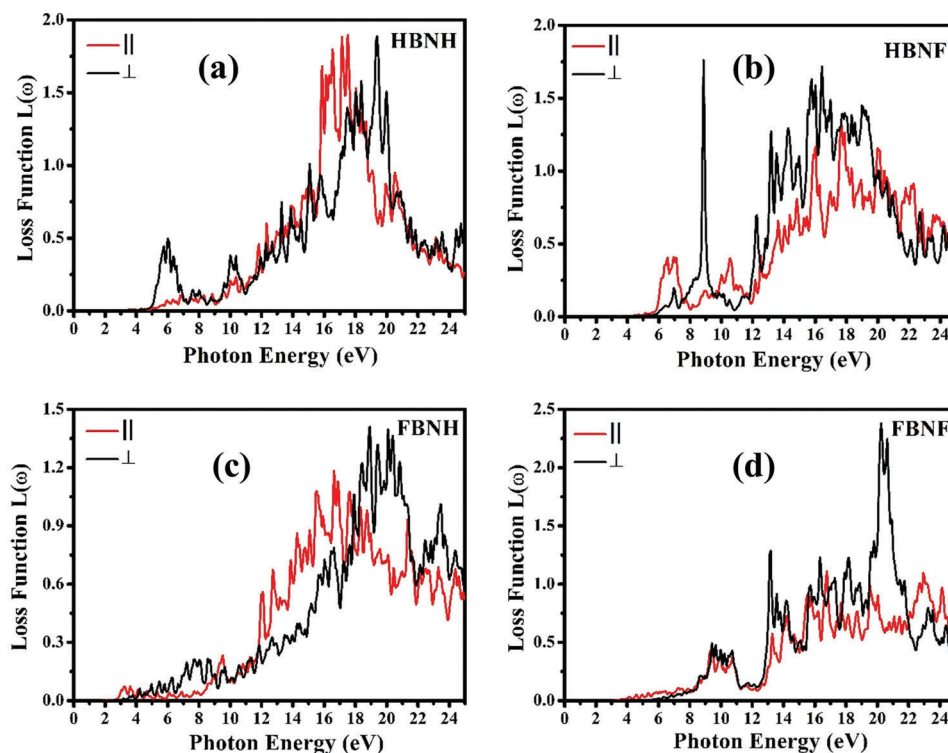


**Figure 10.** Loss function  $L(\omega)$  with the parallel and perpendicular directions of the electric field polarization a) HBNH, b) HBNF, c) FBNH, and d) FBNF.

recombination in device is measured by  $V_{oc}$  and relies on the saturation current and light-generated current. The fill factor known as “FF” calculates the maximal power from studied solar cell device and given by following equation

$$FF = \frac{\vartheta_{oc} - \ln(\vartheta_{oc} + 0.72)}{\vartheta_{oc} + 1}; \quad \vartheta_{oc} = \frac{q \times V_{oc}}{K_B T} \quad (13)$$

In above equation,  $\vartheta_{oc}$  is the normalized  $V_{oc}$ .<sup>[59]</sup> Based on Shockley–Queisser (SQ) limit,  $J_{sc}$  theoretically is evaluated through equation<sup>[28]</sup>

$$J_{sc} = \int q A \varphi \eta_c(E) I_{sun}(E) dE \quad (14)$$

Here,  $I_{sun}(E)$  represents photon flux density taken from AM1.5G spectrum (standard spectrum of Earth’s surface) and  $q$  represents electron charge. In this study, the AM1.5G refers to the air mass coefficient with 1.5 atmospheric thickness, which is equivalent to the straight optical path length in the Earth’s atmosphere at a solar zenith angle of  $z = 48.2^\circ$  with a global tilt in a uniform light source of  $1000 \text{ W m}^{-2}$  for the solar simulator. The values of  $\varphi$  and  $\eta_c$  exhibit weak dependence on the wavelength ( $\lambda$ ), thus Equation (15) can be expressed as<sup>[60]</sup>

$$J_{sc} = \int_0^\infty q A(E) I_{sun}(E) dE \quad (15)$$

where  $A(E)$  denotes absorptivity, based on SQ limit which is 1 for  $E \geq E_g$ , while it is 0 for  $E < E_g$ .<sup>[61]</sup>

The above mentioned solar cell parameters evaluated for HBNH, HBNF, FBNH, and FBNF are tabulated in Table 3.

The development of cost-effective and efficient photovoltaic devices for solar cell applications has driven significant interest in electron-transporting materials (ETMs) based on  $\text{TiO}_2$ . Out of all the metal oxides utilized in nanomaterials,  $\text{TiO}_2$  is particularly noteworthy due to its effectiveness as a charge collector.<sup>[62]</sup> Further, h-BN passivated  $\text{TiO}_2$  semiconductor significantly improves the performance metrics of DSSCs, QDSCs and BHJ solar cells.<sup>[63,64]</sup> Depiction of the process of injecting photoinduced electrons from HBNH, HBNF, FBNH, and FBNF into  $\text{TiO}_2$  surface can be made from Figure 11.

The energy of an electron situated in the ground state of the HBNH, HBNF, FBNH, and FBNF systems, which falls within the  $\text{TiO}_2$  band gap, is raised to an excited state with the assistance of an absorbed photon. After undergoing various processes,

**Table 3.** Solar cell parameters evaluated for all HBNH, HBNF, FBNH, and FBNF.

XBNX	$V_{oc}$ [eV]	FF	$J_{sc}$ [ $\text{mA cm}^{-2}$ ]	$\eta$ [%]
HBNH	4.067	0.980	0.636	2.53
HBNF	4.318	0.981	0.003	0.02
FBNH	3.929	0.979	2.150	8.27
FBNF	3.673	0.977	0.545	1.96

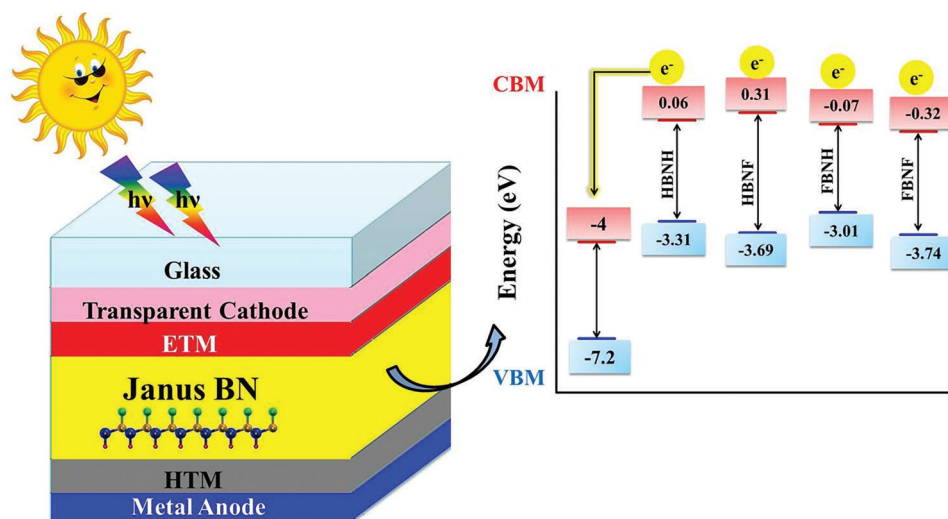


**Figure 11.** Representation of photoinduced electron injection from HBNH, HBNF, FBNH, and FBNF into  $\text{TiO}_2$  ETM.

either adiabatic or non-adiabatic, the excited electron is subsequently introduced into the conduction band of  $\text{TiO}_2$ . It is found that the HBNH, HBNF, FBNH, and FBNF can attach to the  $\text{TiO}_2$  surface using F and H atoms at the edges, leading to a high injection of electrons. Moreover, after analyzing the electronic properties of these systems, we have discovered that the LUMO energies of all HBNH, HBNF, FBNH, and FBNF systems are higher than the conduction band of  $\text{TiO}_2$ . This indicates that the electronic injection from excited states of HBNH, HBNF, FBNH, and FBNF to the conduction band of  $\text{TiO}_2$  occurs more rapidly.

It is seen that material's efficiency can be increased using the alteration of band gap. The increase in energy band gap results in reduced  $J_{sc}$  and enhanced  $V_{oc}$ . Therefore,  $J_{sc}$  and  $V_{oc}$  should be absolute for efficient solar cells. The current–density versus voltage ( $J$ – $V$ ) graphs of HBNH, HBNF, FBHH, and FBNF are shown in **Figure 12**. The total current density is calculated using following equation<sup>[65]</sup>

$$J = J_{sc} - J_0 \left( e^{\frac{qV}{kT}} - 1 \right) \quad (16)$$

where  $J_0$  represents saturation current density that is addition of all recombination mechanisms comprising current density of the Shockley–Read–Hall (SRH), surface, contact, and Auger recombination mechanisms.<sup>[66]</sup> The efficiencies of HBNH and HBNF are 2% and 0.02% respectively. Here, the efficiency of HBNF is almost zero for the reason that in this case the value of  $J_{sc}$  is drastically reduced which is due to its wide band gap as compared to other systems. However, as seen in Table 3, it is noteworthy that values of  $V_{oc}$  and FF are the highest. Therefore, one can further study HBNF to improve its solar properties by adding defects or impurities and various functionalization. The efficiency of Janus FBNH is significantly high in comparison to other considered systems. This enhancement in efficiency of FBNH is due to its high  $J_{sc}$  of  $2.1 \text{ mA cm}^{-2}$  with significantly optimal  $V_{oc}$ . The efficiency of FBNF is lower than HBNH with the value of 1.96%. In this a low  $V_{oc}$  and  $J_{sc}$  are obtained. It is noteworthy that the efficiency of our FBNH is much more as compared to previously re-

ported BHJ solar cell employed h-BN nanoflake-enabled surface passivation on  $\text{TiO}_2$ <sup>[63]</sup> and DSCs consisting of HBN electrode.<sup>[67]</sup> However, our results on FBNH are comparable to DSSC employing h-BN passivated  $\text{TiO}_2$ .<sup>[64]</sup> The efficiency is comparative lower from the lead-free 2D  $\text{CH}_3\text{NH}_3\text{Sn}_{(1-x)}\text{Ge}_x\text{I}_3$  ( $0 \leq x \leq 0.5$ ) perovskites<sup>[68]</sup> and  $(\text{PEA})_2\text{PbI}_4$  and  $(\text{PEA})_2\text{SnI}_4$  2D inorganic–organic hybrid perovskites.<sup>[69]</sup> However, it is well known that perovskites based solar cell faces stability issue and lead toxicity.

While it is true that the comparison between “FBNH” solar cells and “BHJ” or “DSSC” solar cells may not be entirely appropriate due to the differences in material architecture, it is still worth noting that the “FBNH” solar cells have shown noteworthy results in terms of efficiency. This suggests that the development of Janus h-BN materials and their integration into solar cell technology has the potential to offer improvements over existing technologies. Furthermore, the use of Janus h-BN in solar cells presents several advantages, such as its tunable electronic and optical properties, high thermal stability, and compatibility with various substrates. These advantages make Janus h-BN a promising material for next-generation solar cells. As such, continued research and development of Janus h-BN-based solar cells could lead to further improvements in efficiency and stability, which may ultimately lead to the commercialization of this technology. Therefore, we believe that Janus FBNH has properties which are quite encouraging as far its possible application as an absorber layer in solar cells is concerned.

## 4. Conclusion

In summary, we have systematically studied the stability and electronic properties of fully hydrogenated h-BN (H–BN–H), fluorinated h-BN (F–BN–F) and Janus functionalized h-BN (F–BN–H and H–BN–F) employing a first-principles DFT based methodology. The formation energies and phonon dispersion calculations strongly suggest that all considered systems are dynamically stable. It is observed that monolayers HBNH, HBNF, FBNH, and FBNF show semiconducting nature with direct-bandgap of 3.37, 4, 2.94, and 3.42 eV respectively. The direct-bandgap



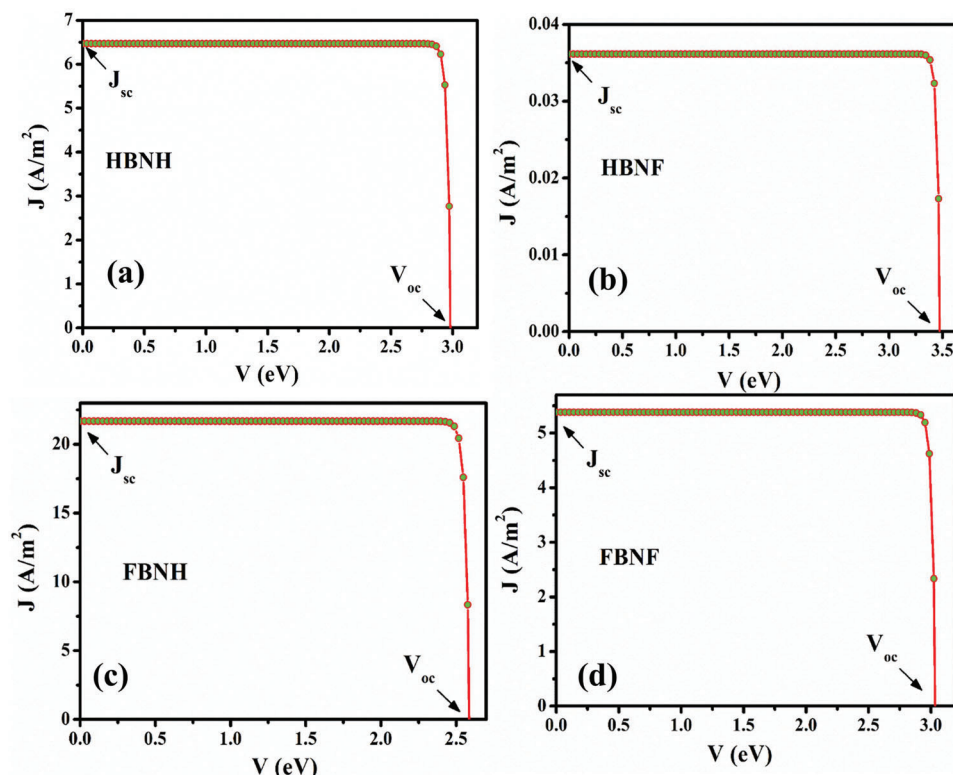


**Figure 12.**  $J$ – $V$  characteristics of a) HBNH, b) HBNF, c) FBNH, and d) FBNF.

semiconducting nature of these systems may have potential application in next-generation nanoelectronics. The solar cell performance of Janus h-BN is examined with respect to power conversion efficiency, short-circuit current density and open-circuit voltage. Among the considered BN systems, FBNH shows superior efficiency with 8.27% with  $J_{sc}$  of  $2.1 \text{ mA cm}^{-2}$ . We strongly believe that our findings could guide future experimental work leading to the possible applications of Janus BN in solar energy devices.

## Acknowledgements

B.R. and V.R. would like to acknowledge the support by Institute Post-Doctoral Fellowship (IPDF) of Indian Institute of Technology Bombay. R.A. and W.L. acknowledge Swedish Research Council (VR-2016-06014 and VR-2020-04410) and J. Gust. Richert stiftelse, Sweden (2021-00665) for financial support.

## Conflict of Interest

The authors declare no conflict of interest.

## Data Availability Statement

The data that support the findings of this study are available from the corresponding author upon reasonable request.

## Keywords

density functional theory, direct bandgap semiconductors, Janus functionalization, phonons, solar cells

Received: January 9, 2023  
Revised: April 16, 2023  
Published online: June 28, 2023

- [1] S. Shukla, S. Y. Kang, S. Saxena, *Appl. Phys. Rev.* **2019**, *6*, 021311.
- [2] V. Sharma, H. L. Kagdada, P. K. Jha, P. Śpiewak, K. J. Kurzydłowski, *Renewable Sustainable Energy Rev.* **2020**, *120*, 109622.
- [3] M. Topsakal, E. Aktürk, S. Ciraci, *Phys. Rev. B* **2009**, *79*, 115442.
- [4] S. Li, M. Sun, J.-P. Chou, J. Wei, H. Xing, A. Hu, *Phys. Chem. Chem. Phys.* **2018**, *20*, 24726.
- [5] K. E. Whitener, *J. Vac. Sci. Technol. A* **2018**, *36*, 05G401.
- [6] J. O. Sofo, A. S. Chaudhari, G. D. Barber, *Phys. Rev. B* **2007**, *75*, 153401.
- [7] Z. Kahrman, M. Yagmurcukardes, H. Sahin, *J. Mater. Res.* **2020**, *35*, 1397.
- [8] C. Casagrande, P. Fabre, E. Raphael, M. Veyssi 'e, *Europhys. Lett.* **1989**, *9*, 251.
- [9] V. Georgakilas, M. Otyepka, A. B. Bourlinos, V. Chandra, N. Kim, K. C. Kemp, P. Hobza, R. Zboril, K. S. Kim, *Chem. Rev.* **2012**, *112*, 6156.
- [10] L. Zhang, J. Yu, M. Yang, Q. Xie, Z. Liu, *Nat. Commun.* **2013**, *4*, 1443.
- [11] C.-F. Fu, J. Sun, Q. Luo, X. Li, W. Hu, J. Yang, *Nano Lett.* **2018**, *18*, 6312.
- [12] M. Idrees, H. U. Din, R. Ali, G. Rehman, T. Hussain, C. V. Nguyen, I. Ahmad, B. Amin, *Phys. Chem. Chem. Phys.* **2019**, *21*, 18612.
- [13] Y. Zhang, B. Sa, N. Miao, J. Zhou, Z. Sun, *J. Mater. Chem. A* **2021**, *9*, 10882.
- [14] Y. Ji, M. Yang, H. Lin, T. Hou, L. Wang, Y. Li, S.-T. Lee, *J. Phys. Chem. C* **2018**, *122*, 3123.
- [15] H. Khatib, *Energy Policy* **2012**, *48*, 737.

- [16] P. Fotis, S. Karkalakos, D. Asteriou, *Energy Econ.* **2017**, 66, 69.
- [17] M. Filippini, L. C. Hunt, *Energy Econ.* **2012**, 34, 1484.
- [18] Y. Jiao, F. Zhang, S. Meng, in *Solar Cells–Dye Sensitized Devices* (Ed: L.A. Kosyachenko), Intechopen, Rijeka, Croatia **2011**, pp. 132–148.
- [19] R. Goodland, H. E. Daly, S. Serafy, B. V. Droste, *Environmentally Sustainable Economic Development: Building on Brundtland*, UNESCO, Paris, France **1991**.
- [20] D. Anderson, S. Winne, *Environ. Dev. Econ.* **2007**, 12, 359.
- [21] R. Cariou, J. Benick, F. Feldmann, O. Höhn, H. Hauser, P. Beutel, N. Razeq, M. Wimplinger, B. Bläsi, D. Lackner, M. Hermle, G. Siefer, S. W. Glunz, A. W. Bett, F. Dimroth, *Nat. Energy* **2018**, 3, 326.
- [22] R. Wang, M. Mujahid, Y. Duan, Z.-K. Wang, J. Xue, Y. Yang, *Adv. Funct. Mater.* **2019**, 29, 1808843.
- [23] M. Grätzel, *J. Photochem. Photobiol., A: Chem.* **2004**, 164, 3.
- [24] A. J. Nozik, M. C. Beard, J. M. Luther, M. Law, R. J. Ellingson, J. C. Johnson, *Chem. Rev.* **2010**, 110, 6873.
- [25] A. Sahu, A. Garg, A. Dixit, *Sol. Energy* **2020**, 203, 210.
- [26] A. Polman, M. Knight, E. C. Garnett, B. Ehrler, W. C. Sinke, *Science* **2016**, 352, aad4424.
- [27] C. Wang, S. Lu, S. Li, S. Wang, X. Lin, J. Zhang, R. Kondrotas, K. Li, C. Chen, J. Tang, *Nano Energy* **2020**, 71, 104577.
- [28] V. Sharma, P. K. Jha, *Sol. Energy Mater. Sol. Cell* **2019**, 200, 109908.
- [29] M. M. Wu, X. Zhong, Q. Wang, Q. Sun, R. Pandey, P. Jena, *J. Phys. Chem. C* **2011**, 115, 23978.
- [30] Y.-T. Liu, X.-M. Xie, X.-Y. Ye, *Chem. Commun.* **2013**, 49, 388.
- [31] W. Shockley, H. J. Queisser, *J. Appl. Phys.* **1961**, 32, 510.
- [32] B. Ehrler, E. Alarcón-Lladó, S. W. Tabernig, T. Veeken, E. C. Garnett, A. Polman, *ACS Energy Lett.* **2020**, 5, 3029.
- [33] P. Giannozzi, S. Baroni, N. Bonini, M. Calandra, R. Car, C. Cavazzoni, D. Ceresoli, G. L. Chiarotti, M. Cococcioni, I. Dabo, A. Dal Corso, S. De Gironcoli, S. Fabris, G. Fratesi, R. Gebauer, U. Gerstmann, C. Gougousis, A. Kokalj, M. Lazzeri, L. Martin–Samos, N. Marzari, F. Mauri, R. Mazzarello, S. Paolini, A. Pasquarello, L. Paulatto, C. Sbraccia, S. Scandolo, G. Sclauzero, A. P. Seitsonen, et al., *J. Phys.: Condens. Matter* **2009**, 21, 395502.
- [34] J. D. Head, M. C. Zerner, *Chem. Phys. Lett.* **1985**, 122, 264.
- [35] J. P. Perdew, K. Burke, M. Ernzerhof, *Phys. Rev. Lett.* **1996**, 77, 3865.
- [36] H. Monkhorst, J. Pack, *Phys. Rev. B* **1976**, 13, 5188.
- [37] S. Baroni, S. De Gironcoli, A. Dal Corso, P. Giannozzi, *Rev. Mod. Phys.* **2001**, 73, 515.
- [38] H. Ehrenreich, M. H. Cohen, *Phys. Rev.* **1959**, 115, 786.
- [39] C. Kittel, *Introduction to Solid State Physics*, John Wiley & Sons, Inc, United States **2010**.
- [40] I. M. Lifshitz, *Zh. Eksp. Teor. Fiz.* **1952**, 22, 475.
- [41] M. S. Dresselhaus, *Physical Properties of Carbon Nanotubes*, Imperial College Press, London **2005**.
- [42] J. Hua, G. M. Vanacore, A. Cepellotti, N. Marzari, A. H. Zewail, *Proc. Natl. Acad. Sci. USA* **2016**, 113, 6555.
- [43] F. Q. Wang, J. Yu, Q. Wang, Y. Kawazoe, P. Jena, *Carbon* **2016**, 105, 424.
- [44] K.-E. Peiponen, E. M. Vartiainen, *Phys. Rev. B* **1991**, 44, 8301.
- [45] B. Roondhe, V. Sharma, H. L. Kagdada, D. K. Singh, T. S. Dasgupta, R. Ahuj, *Appl. Surf. Sci.* **2020**, 533, 147513.
- [46] T. H. Osborn, A. A. Farajian, O. V. Pupyshcheva, R. S. Aga, L. C. Lew Yan Voon, *Chem. Phys. Lett.* **2011**, 511, 101.
- [47] E. Bekyarova, M. E. Itkis, P. Ramesh, C. Berger, M. Sprinkle, W. A. de Heer, R. C. Haddon, *J. Am. Chem. Soc.* **2009**, 131, 1336.
- [48] J. Pellicer-Porres, A. Segura, E. Martínez, A. M. Saitta, A. Polian, J. C. Chervin, B. Canny, *Phys. Rev. B* **2005**, 72, 064301.
- [49] B. Roondhe, S. P. Sanyal, P. K. Jha, R. Ahuja, S. Shukla, S. Saxena, *Appl. Surf. Sci.* **2021**, 556, 149737.
- [50] P. V. Rysselberghe, *J. Phys. Chem.* **1932**, 36, 1152.
- [51] F. Lahourpour, A. Boochani, S. S. Parhizgar, S. M. Elahi, *J. Theor. Appl. Phys.* **2019**, 13, 191.
- [52] D. Singh, S. K. Gupta, Y. Sonvane, I. Lukačević, *J. Mater. Chem.* **2016**, 4, 6386.
- [53] S. Laksari, A. Chahed, N. Abbouni, O. Benhelal, *Comput. Mater. Sci.* **2006**, 38, 223.
- [54] B. Qiu, X. Zhao, G. Hu, W. Yue, J. Ren, X. Yuan, *Nanomater* **2018**, 8, 962.
- [55] L. Yu, A. Zunger, *Phys. Rev. Lett.* **2012**, 108, 068701.
- [56] E. Alamy, A. Bourass, M. Amine, A. Hamidi, M. Bouachrine, *Karbala Int. J. of Mod. Sci.* **2017**, 3, 75.
- [57] M. A. Green, A. Ho-Baillie, H. J. Snaith, *Nat. Photonics* **2014**, 8, 506.
- [58] W.-J. Yin, T. Shi, Y. Yan, *Adv. Matter.* **2014**, 26, 4653.
- [59] M. A. Green, *Solid State Electron.* **1981**, 24, 788.
- [60] M. Guo, K. Xie, J. Lin, Z. Yong, C. T. Yip, L. Zhou, Y. Wang, H. Huang, *Energy Environ. Sci.* **2012**, 5, 988.
- [61] M. J. Patel, D. Raval, S. K. Gupta, P. N. Gajjar, *J. Phys. Chem. Lett.* **2021**, 12, 7319.
- [62] Y. Bai, I. Mora-Seró, F. De Angelis, J. Bisquert, P. Wang, *Chem. Rev.* **2014**, 114, 10095.
- [63] M. Bercx, N. Sarmadian, R. Saniza, B. Partoens, D. Lamoén, *Phys. Chem. Chem. Phys.* **2016**, 18, 20542.
- [64] X. Huang, H. Fu, H. Chen, Z. Lu, D. Ding, Y. Zhao, *J. Appl. Phys.* **2016**, 119, 213101.
- [65] M. Shanmugam, N. Jain, R. Jacobs-Gedrim, Y. Xu, B. Yu, *Appl. Phys. Lett.* **2013**, 103, 243904.
- [66] S. Xu, Y. Luo, W. Zhong, Z. Xiao, X. Liu, *Adv. Mater.* **2012**, 512, 242.
- [67] M. Shanmugam, R. Jacobs-Gedrim, C. Durcan, B. Yu, *Nanoscale* **2013**, 5, 11275.
- [68] M. Kar, R. Sarkar, S. Pal, P. Sarkar, *J. Phys. Chem. C* **2021**, 125, 74.
- [69] M. Kar, A. Ghosh, R. Sarkar, S. Pal, P. Sarkar, *J. Comput. Chem.* **2021**, 42, 1982.